Journal of the European Ceramic Society 43 (2023) 1–13

Contents lists available at ScienceDirect

Journal of the European Ceramic Society

journal homepage: www.elsevier.com/locate/jeurceramsoc

Review article

Reassessing cold sintering in the framework of pressure solution theory

Arnaud Ndayishimiye [a], Sun Hwi Bang [a,b], Christopher.J. Spiers [c], Clive A. Randall [a,b,*]

[a] Materials Research Institute, The Pennsylvania State University, University Park, PA 16802, United States
[b] Department of Materials Science and Engineering, The Pennsylvania State University, University Park, PA 16802, United States
[c] HPT Laboratory, Faculty of Geosciences, Utrecht University, the Netherlands

ARTICLE INFO

Keywords:
Pressure solution creep
Cold sintering
Low-temperature sintering
Densification
Diffusion

ABSTRACT

Cold sintering densification and coarsening mechanisms are considered from the perspective of the non-equilibrium chemo-mechanical process known in Earth Sciences as pressure solution creep (or dissolution-precipitation creep). This is an important mechanism of densification and deformation in many geological rock formations in the Earth's upper crust, and although very slow in nature, it is of direct relevance to the cold sintering process. In cold sintering, we select particulate materials and identify experimental processing parameters to significantly accelerate the kinetics of dissolution-precipitation phenomena, with appropriate consideration of chemistry, applied stress, particle size and temperatures. In the theory of pressure solution, pressure-driven densification is considered to involve the consecutive stages of dissolution at grain contact points, then diffusive transport along the grain boundaries towards open pore surfaces, and then precipitation, all driven by chemical potential gradients. In this study, it is shown that cold sintering of $BaTiO_3$, ZnO and KH_2PO_4 (KDP) ceramic materials proceeds by the same type of serial process, with the pressure solution creep rate being controlled by the slowest kinetic step. This is demonstrated by the values of activation energy (E_a) for densification, which are in good agreement with the existing literature on dissolution, precipitation, or coarsening. The influence of pressure on the morphology of ZnO grains also supports the pressure solution mechanism. Other characteristics that can be understood qualitatively in terms of pressure solution are observed in the in systems such as $BaTiO_3$ and KDP. We further consider activation energies for grain growth with respect to the precipitation process, as well as evidence for coalescence and Ostwald ripening during cold sintering. For completeness we also consider materials that show significant plastic deformation under compression. Our findings point the way for new advances in densification, microstructural control, and reductions in cold sintering pressure, via the use of appropriate transient solvents in metals and hybrid organic-inorganic systems, such as the Methylammonium lead bromide (MAPBr) perovskite.

1. Introduction

Sintering is an important processing step in manufacturing that transitions ensembles of particulate matter into densified polycrystalline bodies using thermal energy, at temperatures below the melting point [1]. Humankind has used this as a fabrication process across the full spectrum of ceramic, polymer and metallic material systems throughout history. Archaeological ceramic artefacts indicate that sintering has been used for over a staggering 26,000 years, back to the upper Paleolithic and early Mesolithic Eras [2]. Over the last 100 years, there have been great intellectual efforts made to understand and advance the sintering process, i.e. to improve microstructure and associated properties via more reproducible production of ceramic and powder metal components [3,4]. Available sintering processes and the associated particulate material technologies have evolved to establish superior densities and more uniform grain microstructures. The sintering techniques developed have varied from hot-pressing, to conventional sintering in furnaces with varying time-temperature schedules, and rates, to microwave sintering, spark plasma sintering, field-assisted sintering, and hydrothermal sintering [5–9]. All the above sintering methods involve a diffusive mass transfer process that thermodynamically lowers the excess surface free energy of the particles/grains, and in doing so removes pores, and develop the granular microstructure. The different stages of the sintering, the nature of the diffusion and the subsequent microstructural development have been considered with theoretical and experimental studies in numerous textbooks and reviews [10–14]. With

* Corresponding author at: Materials Research Institute, The Pennsylvania State University, University Park, PA 16802, United States.
E-mail address: car4@psu.edu (C.A. Randall).

https://doi.org/10.1016/j.jeurceramsoc.2022.09.053
Received 21 June 2022; Received in revised form 27 September 2022; Accepted 28 September 2022
Available online 30 September 2022

some of the more recently introduced sintering techniques, scientific opinion is still developing on the driving forces and mechanisms. This applies especially to the more novel techniques such as spark plasma sintering, microwave sintering, field assisted sintering, and more recently cold sintering. In geological systems such as sedimentary rock, the particulates are typically larger, and thereby involve applied pressures and associated chemical activities, rather than surface energy reduction. In the cold sintering of ceramics, both pressure and surface energy thermodynamic contributions are important as the process is kinetically enabled with a finite applied pressure and appropriate selection of a transient interfacial chemistry.

Cold sintering has been introduced and shown to be an effective method to densify ceramic and metal materials at low temperatures with moderate uniaxial pressures and with an all-important transient chemical phase [15–17], to induce dissolution and precipitation processes. The system being open and with local chemical gradients, means that non-equilibrium conditions support diffusional processes. Conventional sintering processes allow, by definition, the densification of powders at $0.5 \leq T_s/T_m \leq 0.95$, where T_s is the sintering temperature and T_m is the melting temperature of the material. In contrast, densification by cold sintering can be achieved at much lower temperatures, with $0.1 \leq T_s/T_m \leq 0.2$. Such a significant reduction in sintering temperature offers many unique opportunities, such as the co-processing of multi-materials into multilayer devices and new types of nanocomposites permitting the integration of a broad set of material classes and functions [18,19]. The low temperatures also limit deleterious effects such as chemical reactions producing unwanted secondary phases, or decomposition of others, that can hinder functional properties and densification [6]. In addition, the significant drop in processing temperatures offers scope for increasing the sustainability of the sintering step during the fabrication of materials [20].

Despite its advantages, there have been very few attempts to understand the mechanism underlying cold sintering. In the early days of cold sintering, Biesuz et al. introduced a theory of the process [21]. The theoretical analysis mainly leans on a deconvoluted approach based upon earlier ideas developed for sintering by hot pressing (following the Coble creep model) in the presence of a liquid phase, hydrostatically-pressed solid theories and modified Ostwald ripening equations in the presence or absence of an external pressure.

Cold sintering is a geologically-inspired process based on pressure solution creep (PSC) [22]. Historically, it was the British geologist-microscopist Henry C. Sorby, who first reported in 1863 that pressure can enhance chemical reactions, such as dissolution of minerals in an aqueous pore fluid phase, to account for the pitting of pebbles in deformed sedimentary rocks [23]. Later, there was broader appreciation of pressure solution creep, (dis)solution-precipitation creep, or fluid-assisted diffusive mass transfer, which are all terms describing this chemo-mechanical process [24–27]. In the 1950′s, 60′s and 70′s, a number of geologists considered this chemo-mechanical coupling using equilibrium thermodynamic descriptions of the driving force for the phenomenon [28–34]. This provided a physical background to explain many of the observations noted in naturally deformed pelitic, carbonate and other sedimentary and metamorphic rock formations [35,36]; including features such as stylolites, dissolution seams, overgrowths, and indentations at grain contacts. [37] In the geological context, the creep process is extremely slow given the parameters values characteristic of natural rock systems, generally proceeding at strain rates well below 10^{-12} s^{-1} and requiring thousands or tens of thousands of years to achieve significant strains [32]. At first thought, pressure solution therefore seems an unlikely mechanism for underpinning a sintering manufacturing process. However, it is strongly accelerated in fine grained materials and can occur not only in the presence of aqueous intergranular fluids but also in the presence of partial eutectic melt or any intergranular solution phase, provided grain boundaries are wetted [38]. In the ceramics literature, the phenomena was considered by Ashby, Kingery and Coble among others, during the development of structural materials with intergranular phases, but usually at higher temperatures [39]. Similar concepts were also demonstrated on glass ceramics by Raj and Chyung [40]. It is important to note that dissolution-precipitation creep is conceptually similar to conventional solid-state Coble and Nabarro-Herring creep mechanisms, but operates in lower temperature ranges due to the high diffusivity pathways provided by the intergranular solution phase, as shown for example by Rutter [33], and by Urai et al. [41] specifically for rock salt (Fig. 1).

In this work, we reflect on experimental results mainly conducted on $BaTiO_3$ and ZnO ceramics under cold sintering conditions and consider them within the framework of pressure solution creep.

2. Theoretical background on pressure solution creep

The literature on pressure solution creep in stressed granular media, in which grain boundaries and pores host a small amount of a solution phase, has already established that gradients in chemical potential over the surface of grains provide a driving force for intergranular mass transport involving dissolution, diffusion and precipitation [27,29,37,42–48]. The spatial variation in chemical potential drives transport from high potential to low potential sites. In recent years, early equilibrium thermodynamic approaches to quantifying this variation have been extended through more rigorous non-equilibrium treatments, which allow for both static (equilibrium) and dynamic (non-equilibrium) grain boundary wetting by the solution phase, as investigated by Lehner & Bataille [43], Lehner [49], Spiers & Schutjens [50], and Pluymakers & Spiers, for example [51].

On the basis of this work, the mean chemical potential of the solid in an elementary volume of fluid-penetrated grain boundary or particle-particle contact transmitting a normal compressive stress σ_n is approximated by Eq. (1): [33,49,52].

$$\mu_\sigma \approx F_\sigma + \sigma_n \Omega_\sigma \quad (1)$$

Here F_σ is the Helmholtz free energy mainly influenced by changes in elastic and plastic (dislocation-stored) strain energy, Ω_σ is the local molecular volume of the stressed solid. The normal compressive stress σ_n acting at the grain-to-grain (particle-to-particle) contacts is in turn related to the macroscopic normal stress component σ and the pressure

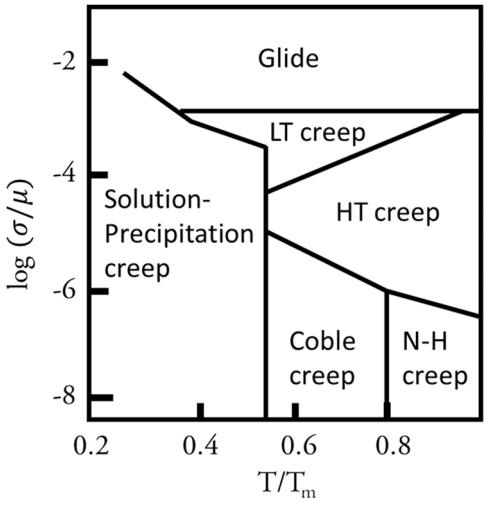

Fig. 1. Deformation mechanism map for rocksalt (NaCl)but typifying a wide range of crystalline materials. Nabarro-Herring (N-H) creep is a stress-driven process controlled by vacancy diffusion within the lattice. Coble creep is a lower temperature process that involves diffusion along grain boundaries. The low temperature and low-stress regime is dominated by the pressure solution creep mechanism, provided this is enabled by a transient chemically active (solution) phase providing a high diffusivity pathway around grain boundaries [41]. https://doi.org/10.1038/324554a0. Copyright 2022 Springer Nature.

P_f of the solution phase in the open pores via Eq. (2): [51].

$$\sigma_n = \frac{(\sigma - P_f)}{R^c} + P_f \quad (2)$$

where σ P is the so called effective normal stress acting in a direction $(- _f)$ normal to the contact considered and R_c is the ratio of the grain-to-grain contact area to grain cross sectional area. Note that all stresses and pressures are measured taking atmospheric pressure as baseline, so that $P_f = 0$ and (2) reduces to $\sigma_n = \sigma / R_c$ when the pore fluid pressure is atmospheric.

In contrast to grain boundary interfaces, the chemical potential in the solid at free pore surfaces corresponds to the equilibrium state between a solid that is under stress and its solution, which is given by Eq. (3):

$$\mu_p \approx F_p + P_f \Omega_p \quad (3)$$

where the local Helmholtz energy F_p and molar volume Ω_p depend on local defect densities and the state of elastic strain.

So, there is an important chemical potential difference between the normally stressed grain boundary and free pore walls, given by Eq. (4):

$$\Delta\mu = \mu_\sigma - \mu_p \approx \left(F_\sigma - F_p\right) + \left(\sigma_n - P_f\right)\Omega \quad (4)$$

assuming that stress-strain related changes in molar volume Ω are negligible. As Paterson highlighted, $F_\sigma - F_p \ll (\sigma_n - P_f)\Omega$ (unless $\sigma_n \approx P_f$) [53], so that Eq. (4) can be simplified as shown in Eq. (5): [45].

$$\Delta\mu \approx \left(\sigma_n - P_f\right)\Omega \quad (5)$$

If $\Delta\mu > 0$, material will be redistributed by diffusive mass transfer from the contacts to the pore regions, through the intergranular solution phase, thereby driving densification. In the case of $\Delta\mu < 0$, there will be transport from the pores into the contacts, thereby cementing the contact regions, via a chemical bonding process [54]. This later case is not considered in the discussion of densification and sintering of brittle ceramic materials.

From the above, it is evident that pressure solution is a coupled mechanical-chemical mechanism driven by grain scale gradients in normal stress and hence chemical potential which lead to a non-equilibrium thermodynamic process [43] involving serial dissolution → transport → precipitation (Fig. 2). At quasi-static, near steady state conditions, the rate limiting (slowest) step amongst these serially coupled kinetic processes controls the densification strain rate [32, 56–59]. The corresponding creep equations for densification of an aggregate of spherical grains containing an intergranular liquid/- solution phase and subjected to an effective stress σ_e (macroscopic

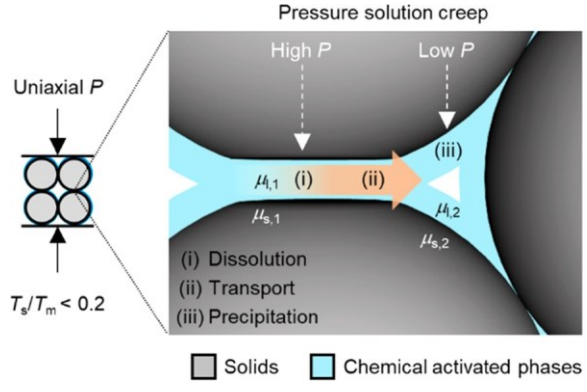

Fig. 2. Schematic illustration of the chemical transformation during cold sintering process based on the results obtained in this study. (i), (ii), and (iii) in the center image represent the serial kinetic processes of dissolution, diffusion (mass transport), and precipitation, respectively [55]. https://doi.org/10.1063/5.0049905. Copyright 2022 AIP Publishing.

applied stress/pressure minus the fluid pressure P_f in the pores) are shown in Eqs. (6)–(8), for dissolution, mass transport and precipitation control, respectively: [56,57].

$$\dot{\varepsilon}_s \approx \frac{k_s}{} \exp\frac{B\sigma_e\Omega}{} - 1 \; f_s(\Phi, e_v) \approx \frac{k_s \, B\sigma_e\Omega}{}{}_s(\Phi, e_v) \quad (6)$$

$$\dot{\varepsilon}_d \approx \frac{DCS}{d}\left[\exp\left(\frac{B\sigma_e\Omega}{RT}\right) - 1\right] f_d(\Phi, e_v) \approx \frac{DCS\, B\sigma_e\Omega}{d^3 RT}{}_d(\Phi, e_v) \quad (7)$$

$$\dot{\varepsilon}_p \approx \frac{k_p}{d}\left[\exp\left(\frac{B\sigma_e\Omega}{RT}\right) - 1\right] f_p(\Phi, e_v) \approx \frac{k_p \, B\sigma_e\Omega}{d \; RT}{}_p(\Phi, e_v) \quad (8)$$

In these relations, $\dot{\varepsilon}_i$ is the volumetric strain for each rate-controlling step (i = s for dissolution, d for grain boundary diffusion and p for precipitation). k_s and k_p are the temperature-dependent rate coefficients for dissolution and precipitation. d is the particle/grain size. D is the diffusivity of ions in the grain boundary fluid phase, C is the solubility of the solid and S is the mean thickness of the fluid film within grain boundaries. Ω is the molar volume of the solid phase, R is the gas constant and T is the absolute temperature. B is a function that depends on volumetric strain (e_v) and initial aggregate porosity-(Φ_0) and expresses stress concentration at grain contacts (a stress intensification factor at grain contacts). $f_x(\Phi_0, e_v)$ is an additional porosity- and strain-dependent geometric term. Calculation details for the functions B and $f_p(\Phi_0, e_v)$ were detailed by Zhang et al. [57] A full derivation of these relations, with the geometric factors expressed in terms of initial porosity and instantaneous porosity, as opposed to initial porosity and volumetric strain, is given by Pluymakers & Spiers [51].

An important prediction of all such relations for densification creep by pressure solution is that the rate controlling process not only depends on the value of the key kinetic parameters, namely k_s, k_p and DCS, at a given temperature, but also on instantaneous aggregate porosity or degree of densification. Specifically, there exists a high porosity region where dissolution controls compaction rate, an intermediate porosity range where diffusion is rate controlling, and a low porosity region where precipitation is rate controlling, as the pore wall area for precipitation tends to zero [51]. In practice, the full sequence of rate controlling processes is only seen when the rates of the three steps are of the same order of magnitude.

3. Stresses in the die during cold sintering

So, the basic processes that underpins pressure solution creep has a number of rate limiting steps, driven by applied stress. With this in mind, we need to consider experimental data obtained in the cold sintering process. Overall, the basic cold sintering process is performed in a heated die. The sample powder is pressed and densified with the aid of a chemical transient phase that is homogeneously added to the starting powder. To ensure that we minimize effects of pressure gradients at the macroscopic (whole sample) scale in assessing the role of pressure solution in the cold sintering process, we select cold sintering studies with on the basis of the sample aspect ratio H/D, where H is the height of the powder and D is the die diameter [60,61]. It is also important that the die surface is flat to insure no shear gradients impact the densification in the die. If is avoided, we can then consider the axial and radial stresses in powder compaction. It is known that under uniaxial compression, there is a radial stress from the force balance at the walls of the die. This problem has been considered with various approaches and across different technologies ranging from ceramics, powder metallurgy, food, and pharmaceuticals [62,63]. Powder pressing or compaction is the principal consolidation methodology offering simplicity, fast processing, and a low-cost approach. Initial compaction of powders in a die can depend on several parameters, including the state of the powder in the form of individual particles, agglomerates, and aggregates, as well as the size distribution. In addition to the particulate form, the pressing rate, the temperature and moisture content can all impact the particle

consolidation, the density, and porosity. There are many earlier non equilibrium models that have been proposed and tested to understand powder consolidation in a die, that is typically used as a forming process.

Of key importance is the pressure transmission that occurs during compaction and under cold sintering. Here the frictional processes of particle-particle and particle-wall frictional interactions control the mechanics. The forces acting in the uniaxial die under compaction can be considered as a force balance expressed as:

$$F_A = F_T + F_F \tag{9}$$

F_T is the transmitted pressure and considered as the force enabling the densification F_F is the force associated with both the die wall friction ($f_w = \mu_w F_R$) and an interparticle frictional contribution ($f_i = \mu_i F_R$), so that.

$$F_A = F_T + F_R(\mu_w + \mu_i) \tag{10}$$

where F_R is the radial force and μ_w and μ_i are (apparent) friction coefficients.

Numerous studies have shown that the radial force, F_R, is proportional to the applied axial force, F_A:

$$F_R = K' F_A \tag{11}$$

where K' is the radial force constant. Long (1960) pointed out that the Poisson ratio, ν, provides the link in terms of principle stresses in a die, such that:

$$\sigma_R = \frac{\nu}{1-\nu}\sigma_A \tag{12}$$

Overall, data associated with die powder compaction accordingly gives a range for $\frac{\sigma_R}{\sigma_A}$ between $\frac{1}{4} \leq \frac{\sigma_R}{\sigma_A} \leq \frac{1}{2}$, so there is a small finite difference in these stresses [64].

Returning to the effects of sample aspect ratio, it is important to note that inhomogeneous pressure gradients can occur during powder compaction in a die. The aspect ratio of the die height (H) to diameter (D) of the powder in the die can impact the stress profile throughout the compacting powder. These gradients have been considered by several authors in terms of H/D ratios. If H< <D, the stress profiles are more uniform, and thereby simplifies the cold sintering studies considered here. We have considered cold sintering in a heated die and targeted data obtained using a uniform stress profile with H ≈ 0.1D [65,66].

4. Cold sintering of ZnO: importance of the solvent and chemical species

In cold sintering, it is known that the process requires the selection of an effective transient chemical additive phase that permits rapid dissolution, mass transport and precipitation, that is a phase that will have reversible solubility, and able to support high concentration solute. To provide sufficient rates of these dissolution process, several approaches can be used: selection of high surface area powders, cosolvents used as part of solvent design, design pH, add chelating agents and raise the temperature under sufficiently high pressures (Although solubility is not universally increased with temperature in all solvents. If there are issues such as the incongruent dissolution then considering solvents with high acidity and alkalinity can be beneficial, along with the use of the common ions effect to balance the different dissolution rates. The selection of the transient phase is non-trivial, but it is essential to enabling the dissolution of sparingly soluble to insoluble chemistries of particles.

Fig. 3a by Bang et al. [67] shows a systematic enhancement of densification under different aqueous solutions with various concentrations of acetic acid. It is known that ZnO has very low levels of solubility in pure H_2O in the neutral *p*H range at low temperatures. In nanoconfined interfaces, this solvent leads to charged ligands ($Zn^{2+}.4H_2O$), as well as more expected ligand with the Zn^{2+} ion surrounded by two water molecules and two hydroxides ($ZnOH_2H_2O$) as discussed by Sengul et al. [17] However, a small concentration of these species can be formed. Therefore, there is little dissolution expected in pure H_2O, and thereby no major densification is seen, at lower temperatures (~150 °C) as expected. There is a small displacement with the heating (Fig. 3a, 0 M, 0.25 M acetic acid), and this is mainly associated with solvent-enhanced particle rearrangement. If acetic acid is added to H_2O, during interactions with ZnO surfaces, Zn^{2+} ions are attached to two acetate molecules and one water molecule $Zn(CH_3CO_2)_2H_2O$. Though the details of complexation mechanisms taking place at the interfaces are non-trivial. This data indicates the all-important design and selection of the transient chemical phase that must be able to initiate the densification under the applied pressure and temperatures. Furthermore, with the higher concentrations of acetic acid, we would expect a pseudo-first order phenomenological rate law (Eq. (13)), as shown by Meulenkamp et al. [68]:

$$-\left(\frac{d[ZnO]}{dt}\right) = K\,[ZnO]^{+} \tag{13}$$

However, it experimentally verified and theoretically confirmed that the presence of important amounts of acetic acid in the system can lead

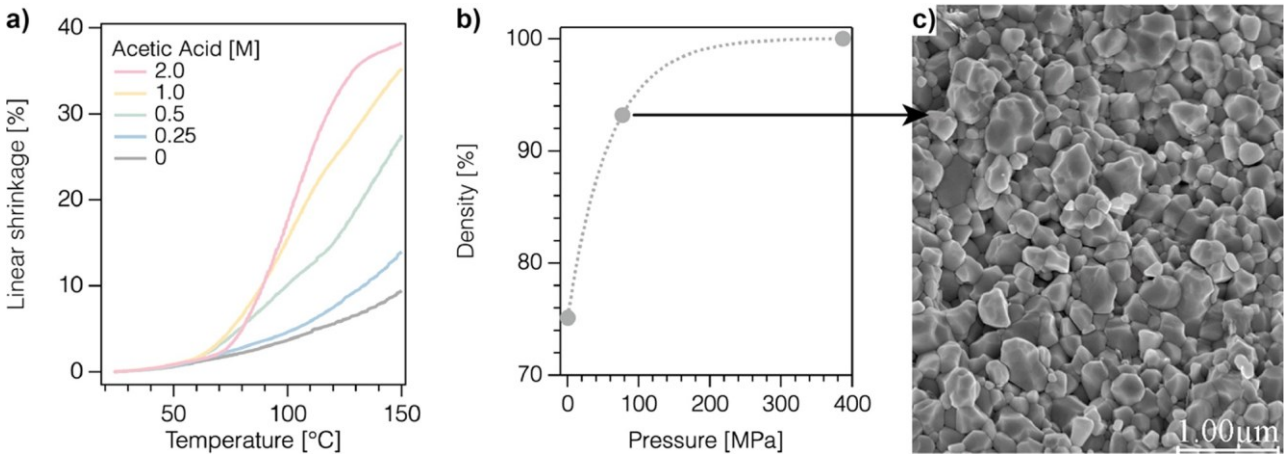

Fig. 3. (a) Linear shrinkage dependence on the concentration of acetic acid [67]. https://doi.org/10.1039/D0TC00395F. Copyright 2022 Royal Society of Chemistry (b) The density trend of the CSP samples with 1 M acetic acid additions sintered at different pressures and (c) the microstructures of the sample cold sintering at a temperature of 126 °C, under 77 MPa for temperature for 1 h [70]. https://doi.org/10.1111/jace.14617. Copyright 2022 John Wiley and Sons.

to limited grain growth, due to a high activation barrier for ligand exchange at the interface [69].

Funahashi et al. showed that there was little to no onset of densification ZnO with 1 mol of acetic acid, until applied pressure of ~70 MPa was applied in the die and heater system, and at higher applied pressure there is increased densification rate (Fig. 3b,c), so here we see the selection of materials and transient chemical phase can significantly drive the chemo-mechanical effect and possibly the pressure solution creep mechanisms [70]. At optimum concentrations of acetic acid, Bang et al. have demonstrated that ZnO could be densified at pressures as low as 27 MPa [71]. This also points to the possibility of a critical pressure enabling cold sintering for given experimental conditions.

5. Energetic aspects and comparison with pressure solution creep processes

5.1. Dissolution process

Fig. 4 shows a non-isothermal densification of ZnO in a cold sintering process after Bang et al. [67]. In this data, the densification rates for various heating rates were considered with the Woolfrey-Bannister analysis [72]. This determined a densification rate for the 2 M-HAc transient chemical phase, with various heating rates between 2.0 and 15.0 °C min^{-1}, under an applied pressure of 175 MPa, and the densification rates are in the intermediate state of the sintering process. The activation energy controlling this densification was found to be $E_a \sim 54$ kJ mol^{-1}. It is also noted that this densification rate is in good agreement with the earlier dissolution rates determined in several publications for the ZnO and acetic acid system, summarized in Table I. In Table I, the activation energies for dissolution range between 38 and 53 kJ mol^{-1} and these average to 46.3 kJ mol^{-1}. In the case of ZnO, with the densification being related to the molarity of the acetic acid, and the activation energy closing matching the dissolution data and thereby consistent with the pressure solution creep controlling high strain rate stages of the densification.

5.2. Precipitation and grain growth

Earlier, we have also considered the grain growth of ZnO under the cold sintering process. We would expect that the kinetics of the grain growth process to be controlled by the precipitation process. In the earlier grain growth study under isothermal conditions, it was shown that

$$G^n - G_0^n = K_0 t \tag{14}$$

where n is an exponent associated with grain growth mechanisms, G_0 is the initial grain size, K_0 is the rate constant with an Arrhenius temperature dependence, and t is time. In the early examples of the cold sintering process, Funahashi et al. [70] have determined an exponent of

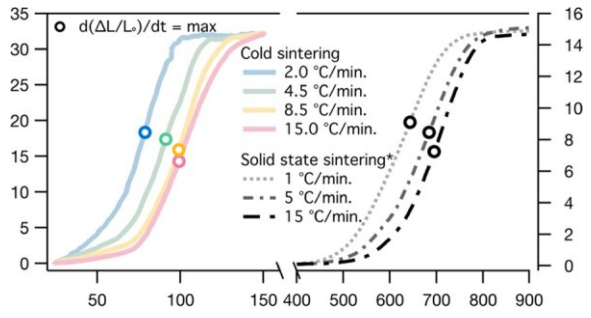

Fig. 4. Linear shrinkage of ZnO cold sintering and solid state sintering process using various heating rates [67]. https://doi.org/10.1039/D0TC00395F. Copyright 2022 Royal Society of Chemistry.

Table I
Activation energy (E_a) for dissolution in different ZnO-Acetic acid systems.

E_a for dissolution (kJ mol^{-1})	Comments	References
38	Nanopowder-ZnO	Meulenkamp et al. [68]
45		Gerischer et al. [73]
48		Hurs, it et al. [74]
53		Blinkova et al. [75]
47.6	Trichloroacetic acid	Deng et al. [76]

$n = 3$ for the case of ZnO undergoing cold sintering with an acetic acid transient phase and over temperatures between 120 and 300 °C, and under an applied uniaxial pressure of 77 MPa [70]. However, the activation energy for the grain growth, E_a, determined from the rate constant was found to be 43 ± 2 kJ mol^{-1}. This was much smaller than the typical activation energies for grain growth kinetics as reported in conventional sintering studies in ZnO systems. Table II shows a comparison of ZnO grain growth investigation under the extensive earlier conventional sintering studies, where the average ~ 250 kJ mol^{-1} [77–81]. With such large differences in the activation energies between conventional sintering and cold sintering, we must anticipate different controlling mechanisms between these processes.

Following a ramp rate of 15 °C/min and under a uniaxial pressure of 175 MPa, we considered the microstructural evolution of cold sintering of ZnO under an isothermal 150 °C condition. These samples are then analyzed with transmission electron microscopy to reveal a very thin amorphous phase between the ZnO grains, as well as metal-organic phases in pores [82]. With various hold times, there is a thinning out of the intergranular phase, shrinkage of the pores, and grain growth all within a 30 min hold at this temperature. Fig. 5 show the microstructural evolution under these isothermal conditions via transmission electron microscopy analysis at the 0- and 30-minute points along the isothermal hold at 150 °C, reported by Bang et al. [82]. The start of the isothermal dwell was defined as the point at 9 min where densification reaches a threshold. In this window, the grain sizes increase from 109 to 184 nm in the 30 min at 150 °C. This would suggest there are diffusional fluxes both along but also perpendicular to the interfaces, through i) decomposition of residual interfacial phases, and ii) reprecipitation of ZnO following the reverse zinc oxide to zinc acetate reaction, as highlighted by Sengul et al. [83].

Various additional insights can be gained from experiments and observations on the microstructural evolution of cold sintered ZnO in the final stages of the cold sintering process, where we have relative densities greater than 93%. From the observation of a thin amorphous intergranular phase, we identify a transient residual phase that likely controls solute exchange along the grain boundaries and into the pores. This interfacial reaction in ZnO at low temperatures is therefore more akin to solution particle synthesis and associated coarsening processes, than traditional solid state grain growth. So, with ZnO particle growth from solution the activation energies are summarized from several studies in Table III [84–89]. These activation energies, which range between 23 and 71 kJ/mol, average out to 39.6 kJ/mol, and therefore are very much like the earlier grain growth activation energy of 43 ± 3 kJ/mol reported by Funahashi et al. [70]. So, this suggests that in

Table II
Activation energy (E_a)for grain growth in conventionally sintered ZnO and mechanistically controlled by volume diffusion mechanisms as n = 3.

E_a for grain growth (kJ mol^{-1})	n exponent	Comments	References
409	3	Undoped	Nicholson et al.[77]
253 ± 42	3	Undoped	Gupta et al.[78]
213	3	Undoped	Dutta et al.[79]
224 ± 16	3	Undoped	Senda et al.[80]
150 ± 25	3.5	Bi_2O_3 - doped	Han et al.[81]

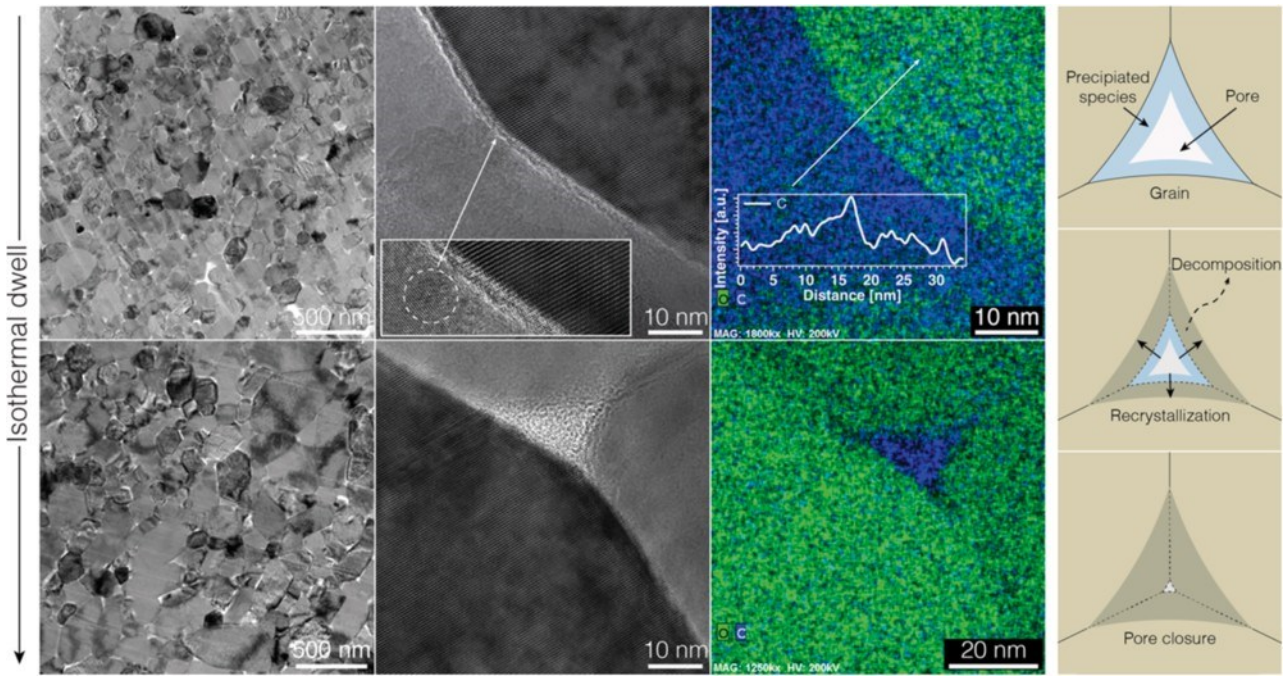

Fig. 5. Microstructure and EDS mapping at the 0- and 30-minute of isothermal dwell [82]. https://doi.org/10.1016/j.mtchem.2022.100925. Copyright 2022 Elsevier.

Table III
Activation energy (E_a) for ZnO particle growth with various synthesis techniques.

E_a for particle growth (kJ mol^{-1})	Comments	References
34	$Zn(CH_3CO_2)_2$ Ostwald Ripening with n = 3	Hu et al.[84]
24 ± 3	Undoped ZnO	Ingham et al.[85]
43 ± 4	Al-doped ZnO with sol-gel	Ingham et al.[85]
23 ± 2	ZnO crystal growth from an amorphous film	Bouhssira et al. [86]
71		Viswanatha et al. [87]
35	Hydrothermal ZnO Nanowires	Cheng et al.[88]
46.8	Hybrid Growth Process	Liu[89]

Table IV
Names of ZnO samples prepared by CS with a $H_2O/Zn(acac)_2$ chelate mixture, from Ndayishimiye et al. [90].

Sample name	Pressure (MPa)	Temperature (°C)	Time (min)	Type of sample / Processing details
ZnO – RT	350	25 (Room temperature)	0	Reference sample Compacted ZnO + Zn $(acac)_2$ powder
ZnO – 100	350	100	0	Sample quenched after the system reached 100 °C
ZnO – 140 A	350	140	0	Sample quenched after the system reached 140 °C
ZnO – 140B	350	140	120	Sample obtained after a 120 min dwell at 140 °C

the temperature window for grain growth, there is an interfacial precipitation reaction that controls the coarsening.

5.3. *Coarsening mixed modes during cold sintering*

The evolution of the grain size distribution of ZnO cold sintered with a water/ zinc acetylacetonate hydrate chelate (*$H_2O/Zn(acac)_2$*) mixture, under an applied pressure of 350 MPa and quenched at different densification steps (Table IV) is shown in Fig. 6.

The grain size distribution shows a coarsening with a series of broadening size distributions. This distribution trend is consistent with a mixed mode of coarsening, as shown Takajo et al. in an extensive statistical study [91]. Coarsening of grains can be driven by two mechanisms: Ostwald ripening and coalescence. The basic difference between coalescence and Ostwald ripening is that in coalescence, small particles/grains combine to form a large grain whereas, in Ostwald ripening, small particles dissolve in a solution and then reprecipitate to form large particles/grains.

In summary, across all these various approaches to investigate the coarsening of ZnO by cold sintering, the activation energies are significantly low in comparison to the solid-state sintering, and in good agreement with values associated with ZnO dissolution and surface diffusion-limited growth. During the latest stages of sintering, coarsening can occur through Ostwald Ripening and coalescence mixed modes.

6. Non-equilibrium thermodynamics in cold sintering

During pressure solution, grain boundaries are having a absorbed interface, that can evolve dynamically to a rough topography of contact asperities (islands) separated by a network of fluid-filled channel structures (Fig. 7a), in line with expectations from non-equilibrium thermodynamics according to Lehner and Bataille [43]. When subjected to high stresses, grain boundaries remain dynamically wetted as contact asperities continuously undergo dissolution and precipitation without attaining thermodynamic equilibrium [92,93]. The specifics of these intergranular structures are dependent on the respective crystal orientations across the contacts across adjacent particle.

Van Noort et al. considered the healing of these island-channel structures at the nanometer scale, i.e. the formation of isolated fluid inclusions within grain boundaries, and dihedral angles within intergranular pores, in the approach to equilibrium as stress levels decrease

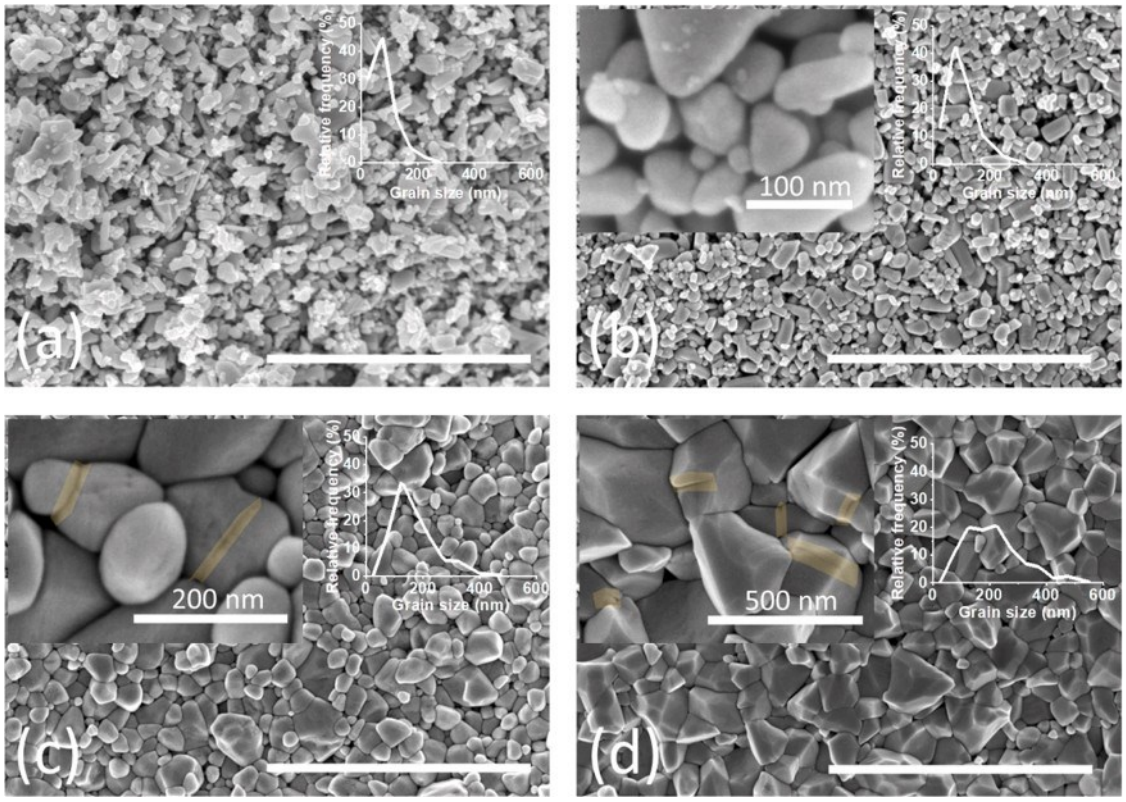

Fig. 6. SEM Images and grain size distribution of (a) ZnO-RT, (b) ZnO-100; inset: high magnification image showing nuclei on grain surfaces, (c) ZnO-140A and (d) ZnO-140B. In (c) and (d), the zones highlighted in yellow show coalescence features between grains during the sintering process. Scale: 2 μm, unless otherwise noted.

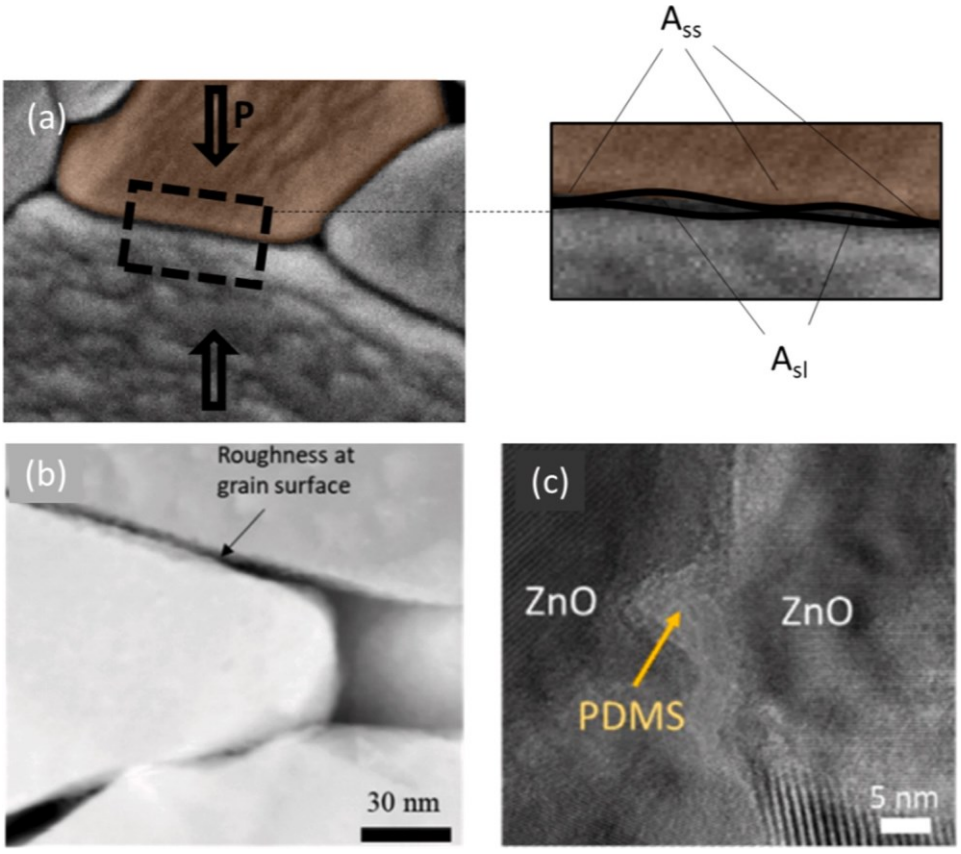

Fig. 7. Grain-Grain contacts during pressure solution exhibiting roughness with: Ass: area of the solid-solid asperity contacts and Asl: solid-interfacial liquid interfaces. The image is readapted from van den Ende et al. [92]. https://doi.org/10.1029/2019JB017500. Copyright 2022 John Wiley and Sons (b) HAADF of a hydrothermally sintered ZnO [95], and (c) HR-TEM image of a cold sintered ZnO-PDMS composite [96]. https://doi.org/10.1016/j.jeurceramsoc.2019.11.049. Copyright 2022 Elsevier.

[94]. The local non-equilibrium nature and high surface energy of rough interfaces and island-channel structures will provide an additional driving force for mechanisms such as coarsening.

Indeed, several SEM (Fig. 6c) and TEM micrographs (Fig. 7b) confirmed the existence of interfacial roughness at grain boundaries during densification of ZnO by cold sintering [55,95]. Furthermore, it was recently shown that when polymers are added to form new types of grain boundary interfaces to fabricate new nanocomposites, the grain boundary mobility decreases, due to diffusional processes being inhibited from the inert polymer phase. This slows down recrystallization and mass redistribution processes, also leading to grain boundaries with high roughness grain boundaries as shown in Fig. 7c [96].

7. Visual evidence of pressure solution creep

$BaTiO_3$ was cold sintered using $(SrOH_2).8\ H_2O$ as a transient phase. This strongly alkali chemical phase drives a dissolution of both the Ba^{2+} ions and Ti-O suboxide species into the flux. The Sr^{2+} ions compete with the Ba^{2+} to react with Ti-O species before both undergoing precipitation. The distribution of Sr observed in the STEM-EDS map (Fig. 8a-b) suggests that the precipitation of $Ba_{1-x}Sr_xTiO_3$ strongly depends on the direction of pressure. Grain boundaries orthogonal to the direction of pressure contain less Sr than non-orthogonal ones. Indeed, the first configuration has high local stresses enabling an easy interfacial liquid phase elimination.

This then leads to an anisotropy in the width of a shell region to the is linked with the axial, and radial stresses led to a concentration gradient difference between the two principal stress axes (Fig. 8a-c). The schematic diagram of the mechanism is shown in Fig. 8c-d.

In the case of $BaTiO_3$ cold sintering using NaOH-KOH eutectic flux, the densification and microstructural control are much easier, compared to other sintering methods [98]. After sintering, the $BaTiO_3$ highlights a dense microstructure composed of faceted nanograins (Fig. 9a). In the example shown here, the starting $BaTiO_3$ powders have hydroxyl inclusions with local precipitates within the lattice, originating resulting from conditions used during their hydrothermal synthesis. Within different grains, a shell region that is largely free of these hydroxyl precipitates as observed (Fig. 9b, c). This would be consistent with epitaxial growth on $BaTiO_3$ surfaces during precipitation. The temperatures are so low that there is no lattice diffusion to remove the residual defects from inside the grains. The initial average particle size for the $BaTiO_3$ was 20 nm, and with isothermal holds at 350 MPa for 12 h. We also assume that the amount of flux may influence the dissolution-precipitation reaction yield, thus the kinetic of grain growth through Ostwald ripening as final grain sizes are 75 nm and 150 nm for 4 and 6 wt% NaOH-KOH, respectively. Evidence for coalescence in the

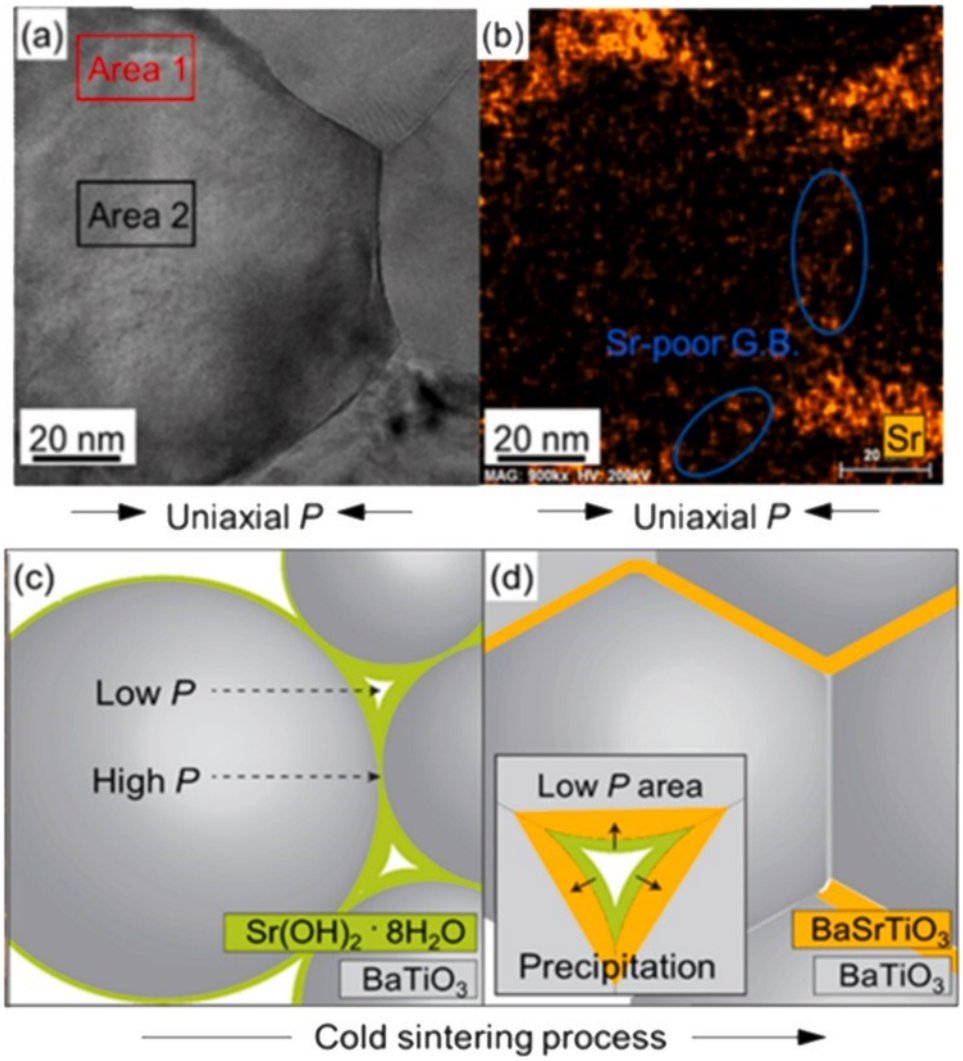

Fig. 8. (a) TEM image of $BaTiO_3$ cold sintered with $Sr(OH)_28\ H_2O$ and (b) the corresponding STEM-EDS elemental map for strontium (Sr). (c)and (d) Schematic diagrams of the $Ba_{1-x}Sr_xTiO_3$ precipitation and epitaxial growth during cold sintering [97]. https://doi.org/10.1111/jace.17461. Copyright 2022 John Wiley and Sons.

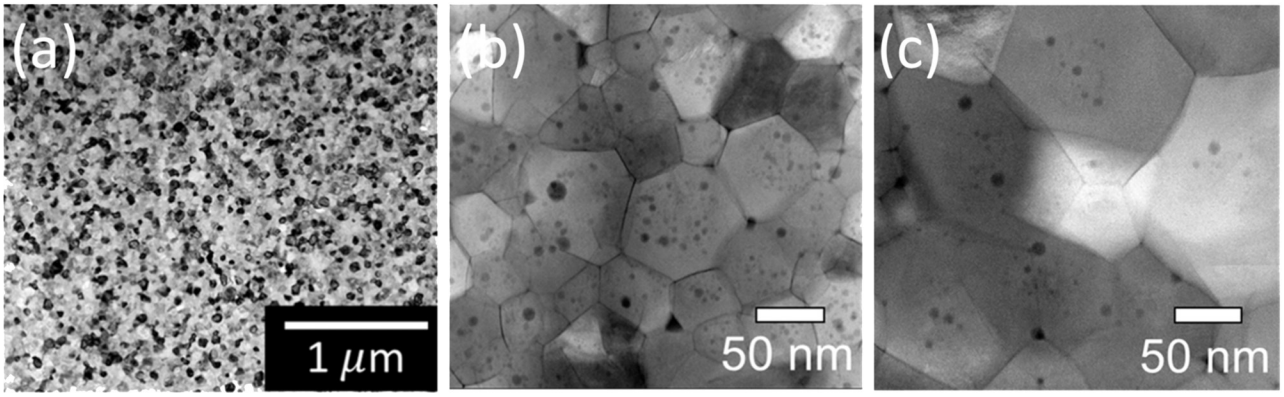

Fig. 9. (a) TEM image and (b) STEM image of $BaTiO_3$ cold sintered with 4 wt% NaOH-KOH. (c) STEM image of $BaTiO_3$ cold sintered with 6 wt% NaOH-KOH. [100] https://doi.org/10.1016/j.jeurceramsoc.2019.12.022. Copyright 2022 Elsevier.

$BaTiO_3$ case has at this time not been found. The transient and complex pathways that enables the dissolution and precipitation was considered in detail for the $BaTiO_3$ surface in contact with a molten KOH-NaOH flux, that shows the formation of intermediate and unstable complexes formed by destabilizing and breaking rate-limiting Ti – O bonds within the perovskite [99].

7.1. Ongoing in situ investigations

7.1.1. X-Ray adsorption Spectroscopy

KH_2PO_4 (KDP) has low X-ray adsorption and is there for a model system for in-situ cold sintering ultra-small (USAXS) and small angle x-ray scattering (SAXS)and can be a powerful method to understand the evolution of the densification, especially with respect to the pore size under different pressures, temperatures, and times, the basic process is shown in Fig. 10. A 30% volume reduction was determined. Also, the pore surfaces are found to have an interface that decreases from ~ 4–0.4 nm as the water is evaporated during KDP densification by cold sintering. This method with modeling is very effective in addressing the detailed evolution of various interfaces during cold sintering. There was also evidence for interfacial pores that could be related to the island structures that was proposed by van Noort et al. in the more advanced pressures solution creep models [94].

7.2. Evolution of the contact area during cold sintering

In pressure solution, the dissolution of solids into the transient chemical intergranular phase is enhanced by the application of an external uniaxial stress. When modeled on spherical grains with a diameter d, packed in a cubic arrangement, it is known that: (i) at zero strain, the contact area between particles is zero and (ii) the contact area at a strain ε, the grain-grain contact which accumulates post elastic creep, becomes a circle that grows larger with ε [57]. The matter removed from the truncated spheres by dissolution is precipitated in pore walls. The contact area A_c and strain ε can be defined by Eq. (15): [57].

$$A_c = 6\pi\ r^2 - x^2) \tag{15}$$

where r is the grain radius measured from the grain center to pore wall, and x is the distance between the grain center and the grain boundary at strain ε. x can be obtained with Eq. (16) and r can be obtained by solving Eq. (17):

$$x = \frac{d}{2}(1-\varepsilon)^{\frac{1}{3}} \tag{16}$$

$$-2r^3 + 4.5r^2x - 1.3x - \frac{d}{2} = 0 \tag{17}$$

Fig. 11a shows the evolution of strain with time during the cold sintering of $BaTiO_3$. By assuming the grain size invariant during sintering (d= 91 ± 37 nm) and $r \sim d/2$, the subsequent contact area A_c at different was estimated by using Eqs. (15) and (16). The contact area rapidly increases by two orders of magnitude, up to a value estimated at 9.0×10^{-15} m [2] (Fig. 11b). This value is within a similar order of magnitude from the average contact area (6.8×10^{-15} m²) estimated from more than 40 facets in the $BaTiO_3$ microstructure shown in Fig. 11c. The stress intensification factor B, which gives an insight on the actual local stresses at particle or grain contacts during sintering can be estimated using Eq. (18): [57].

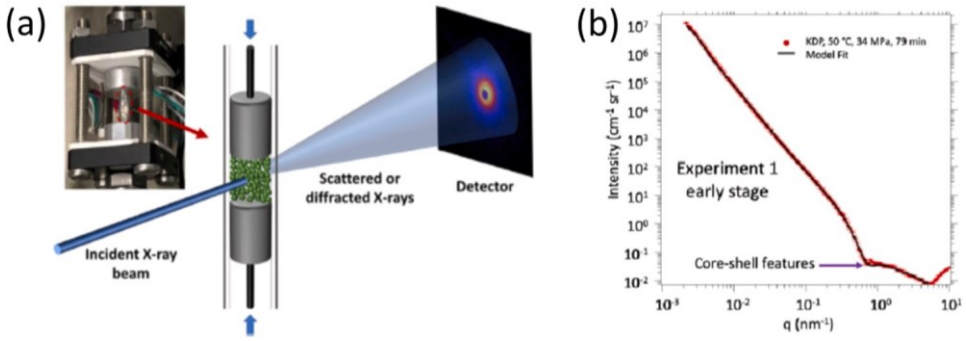

Fig. 10. (a) Cold sintering compression cell composed of a thin quartz capillary containing the sample for X-Ray studies, stainless steel pistons mounted in a uniaxial press TEM image and (b) Microstructural model vs combined USAXS/SAXS slit-smeared data obtained during cold sintering [101]. https://doi.org/10.1111/-jace.17664. Copyright 2022 John Wiley and Sons.

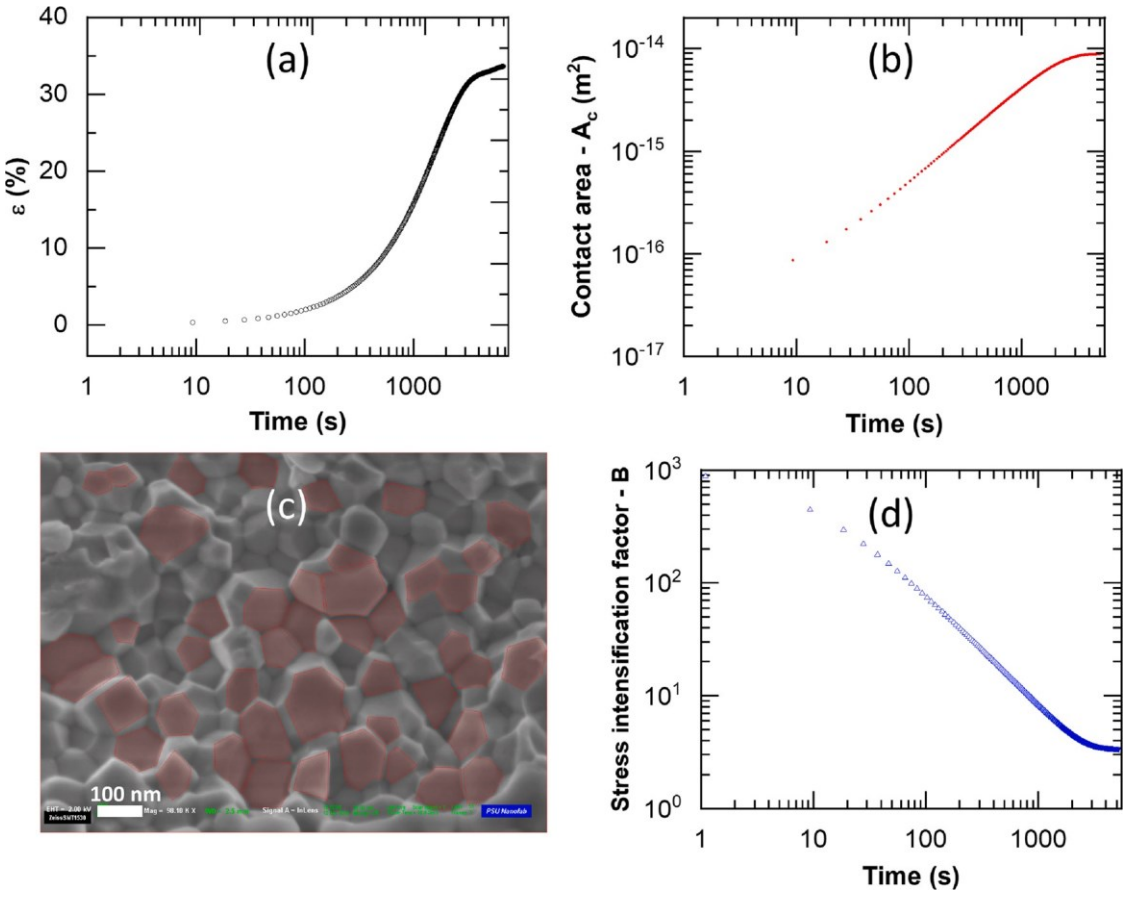

Fig. 11. $BaTiO_3$ time-dependent evolution of (a) strain ε, (b) contact area A_c with the corresponding SEM image (c) where facets (areas in red) are selected to estimate the experimentally-observed contact areas after cold sintering, and (d) stress intensification factor – B.

$$B = \frac{6d^2(1-\varepsilon)^{\frac{2}{3}}}{A_c} \tag{18}$$

Fig. 11d highlights that B is nearly 900 at the beginning of cold sintering, which would correspond to almost 300 GPa of local stress. However, B rapidly decrease towards single digits in less than 20 min. Indeed, the stress redistribution across expanding inter-granular contacts which is one of the factors leading to the slowdown of pressure solution [102]. In the applied experimental conditions, the chemical compaction equilibrium is reached when B ~ 3.

8. Systems with a minor pressure solution component in the densification

Under compaction of materials such as organic crystals, organic-inorganic perovskites, and metals the major densification is due to plastic deformation processes. Some, of the earlier work on this were published by H. de Beauvoir, Josse et al., demonstrating that metastable magnetic molecular crystal mixed with a small amount of solvent could be sintered using a Spark Plasma Sintering (SPS) apparatus at very low temperatures [103]. This approach was referred to as cool SPS, and can either operate in the presence of structural or added H_2O [104,105]. Here we consider two cases with plastic deformation processes: metals and molecular hybrid organic-inorganic perovskite methylammonium lead bromide (MAPBr) used for solar cells. and as the also under compaction stresses. Fig. 12a shows that with the addition of a chemical additive there is an additional densification process over the plastic deformation in a ferrous powder metal. EDS mapping (Fig. 12b-e) highlights that the chemical additive (H_3PO_4 in this example) reacts with iron to form a thin iron phosphate interface between grains. Although the chemically enhance densification is only a small percentage of the overall densification, it led to significant increases in the cohesion strength relative to the conventional warm compaction of powders [106].

Hybrid organic inorganic perovskites such as MAPBr, can undergo plastic deformation, but the grain microstructure and densification can be significantly improved with the addition of appropriate organic solvents, under a pressure heating process [107]. SEM images show that without a liquid/transport phase, the dry pressed material is porous and has a heterogeneous grain size (Fig. 12f). However, with the various transient chemistries (Fig. 12g-k) such as 2-methoxyethanol (2-MOE), γ-butyrolactone (GBL), dimethylformamide (DMF), dimethyl sulfoxide (DMSO) and Pb-hydrated acetate ($Pb(OAc)_2 0.3\ H_2O$), there is a sintering with a more faceted microstructure and the applied stress can be significant reduced. The advantages all being improved with the enhanced diffusion that is linked to the chemo-mechanical processes that underpin pressure solution creep.

9. Cold sintering hybrid methodologies

With so many recent innovations in sintering approaches including variations of field assisted sintering, it is no surprise that transient chemical phases have been added to the pre-sintered powders to consider hybrid methods to take advantage of sintering. In a forward-thinking review, Biesuz et al. correctly points out that there are multiple coupling mechanisms that can drive the diffusion processes in a new era of sustainable sintering methodologies [108].

This generalist few is supported with recent studies by Julian-Gonzalez, Guillon et al. [109] on water assisted SPS of ZnO; H. de Beauvoir et al. with solvent-assisted SPS of metastable materials at low

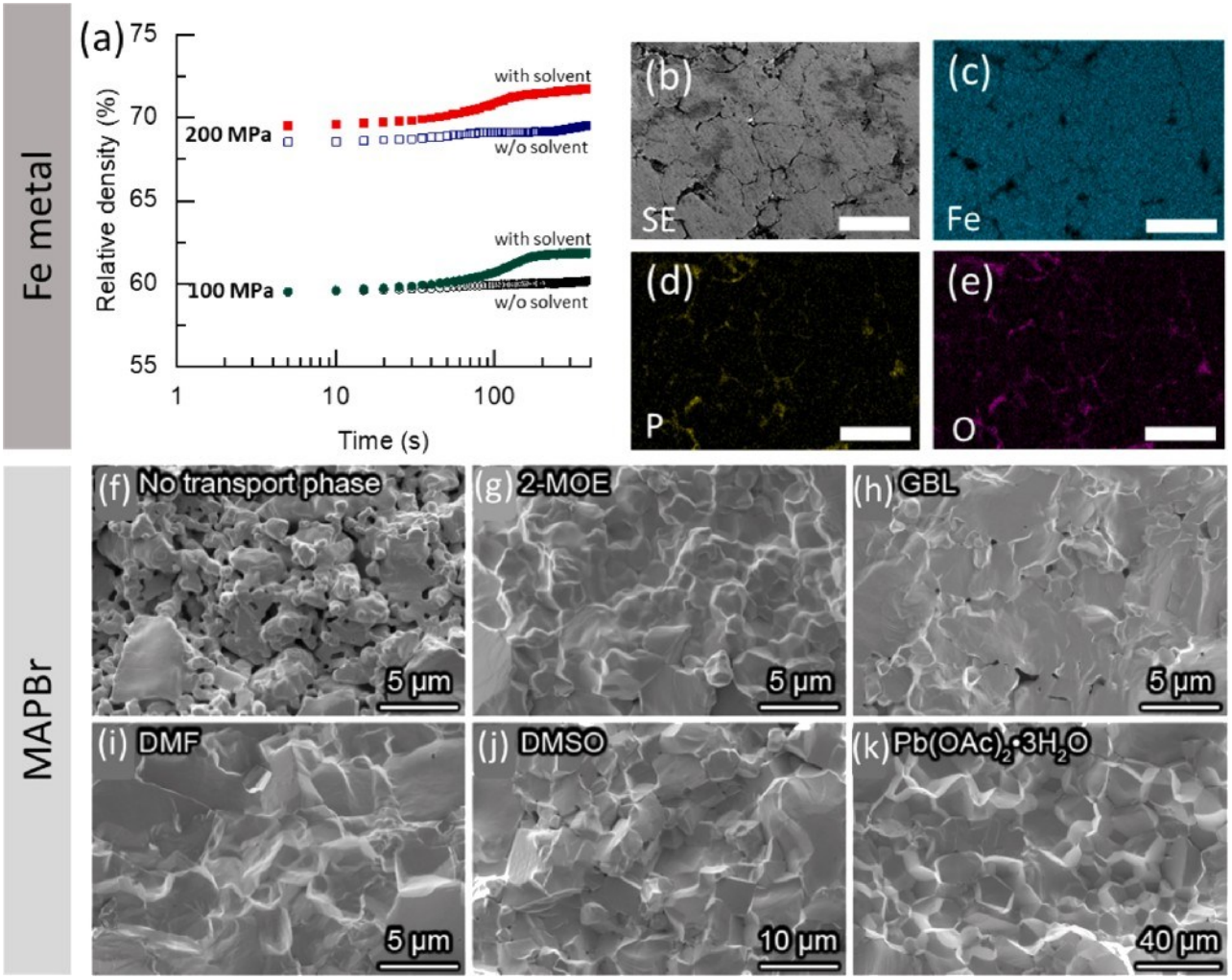

Fig. 12. (a) Densification behavior of iron at different pressures with or without (w/o) a solvent. EDS analysis of a Fe metal cold sintered using H_3PO_4, with simultaneous acquisition of: (b) Secondary electron (SE) image and elemental maps of (c) iron (Fe), (d) phosphorous (P) and (e) oxygen (O). Scale bar: 50 µm. SEM micrographs of MAPBr samples cold-sintered (f) without a liquid phase, (g-k) with various transient chemistries. The microstructure and grain growth differences is apparent and impacted with different selections solvent chemistries [107].

temperatures [110] and acetic acid assisted Flash Sintering of ZnO from Luo et al. [111]. In these cases, the preheating of the powders before the application of the electric field could be significantly reduced that are typically required to drive semiconductor carrier concentrations up to then initiate the joule heating process. Building on these concepts, Guo et al. conducted a comprehensive SPS and CSPS study determining the energetics if the sintering process about both densification and grain growth studies in ZnO [112]. Fig. 13b,c shows the grain growth kinetics of these two sintering approaches, we note that the SPS is in good agreement with the conventional grain growth activation energies, with

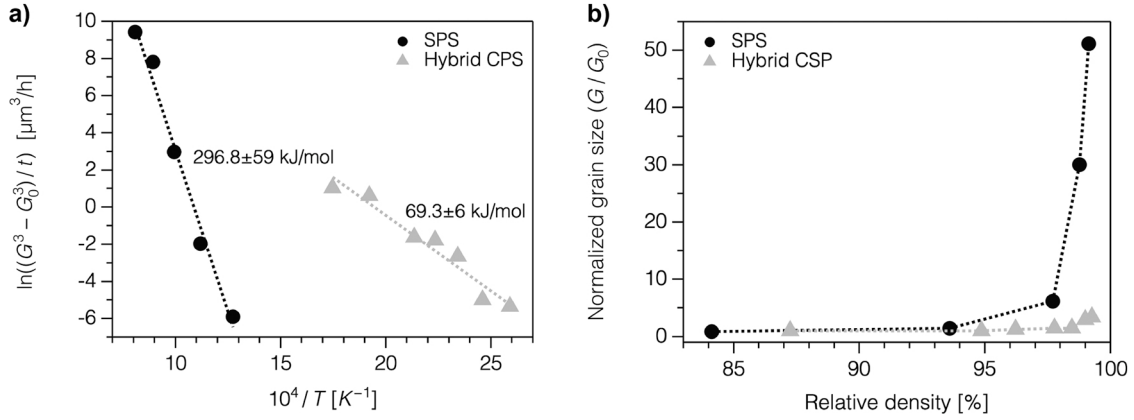

Fig. 13. (a) Activation energies for grain growth and normalized grain sizes to estimate the extent of coarsening during CSPS and SPS. [112].

296.8 ± 59 kJ mol^{-1} with n = 3, but the hybrid CSPS as would be expected have a much lower activation energy, as we have seen in simple cold sintering processes as we discussed above. Here the activation energy is found to be 69 ± 6 kJ mol^{-1}, and n = 3. The mean grain sizes are limited to short times, 5 min soaking time for these studies and therefore the coalescence is suppressed, and the high standard deviations in grain size are minimized. The pressure (50 MPa) is also low relative to the classic cold sintering cases. With the activation energy controlling the grain growth being little higher for the hybrid CSPS case than with our earlier cold sintering data. It is also interesting to note the density -grain size variation for the two methods, both SPS and CSPS are excellent in driving densification and suppressing grain growth under these conditions, but the CSPS is the most effective, with limited growth under these conditions and relative densities above 99%.

This shows that the basic ideas behind the most recent methods of sintering can be enriched in the presence of solvents as sintering aid, in combination with applied pressure. It indeed helps to increase in the diffusional processes that enabling the densification of materials. The details and energetic of all these processes are still developing, but it is certain that the pressure solution creep processes are providing a convenient trigger to these hybrid methods, and the result is a continued lowering of the input energy that is need for sintering.

10. Summary and conclusions

The aim of this article is to converge the science of geological pressure solution creep with solvent- and pressure- assisted low temperature sintering techniques such as cold sintering. It is noted that the detailed fundamental understanding of cold sintering is still a work in progress, given its recent discovery. Despite this, the present article links the various aspects of the chemo-mechanical diffusional processes associated with pressure solution creep to the cold sintering process in what we feel is a very insightful way. It is generally agreed there is a complex process that requires the sequential mechanisms of dissolution, grain boundary diffusion, and precipitation to minimize the excess surface energy of particles in a densification. Here, we have gained insight into determining rate limiting steps associated with different stages of the sintering of ZnO, under certain experimental conditions. The densification process in the ZnO/acetic acid system by cold sintering has activation energies in good agreement with the ZnO dissolution process. The grain growth rates are also in good agreement with diffusion-controlled rates as n = 3, and with activation energies that are much very smaller than the traditional solid-state sintering. The calculated activation energies for grain growth are more in line with energetic values seen for particle growth during chemical synthesis. During the CSP of ZnO, besides microstructural evidence, a significant broadening of the size distribution is observed with time. This is consistent with a mixed coarsening mode involving both Ostwald ripening and coalescence. We also consider several other materials that have undergone cold sintering and examine the pressure solution creep mechanism as one that accounts for the microstructural development - specifically a small chemical reprecipitation anisotropy relative to the applied axial pressure that can be detected in the microstructure of Sr-doped $BaTiO_3$ densified with an alkali component flux. This shows more precipitation in directions perpendicular to the axially applied pressure than parallel. We hope that for future publications that address the mechanisms underpinning various cold sintering stages, and in different materials, this article will aid the research debate, and help science progress to more comprehensively understand the details of the diffusional process that enables the densification, as well as decoupling the contributions of dissolution, mass transport and precipitation throughout the cold sintering process, and the roles of applied stress versus surface energy driving forces.

Declaration of Competing Interest

The authors declare the following financial interests/personal relationships which may be considered as potential competing interests: Clive Randall reports financial support was provided by National Science Foundation. Clive Randall reports financial support was provided by Air Force Office of Scientific Research. Clive Randall has patent #10730803 issued to Center for Dielectrics and Piezoelectrics.

Acknowledgments

We would like to acknowledge support from the National Science Foundation, grant numbers DMR-1729634 (student funded: Sun Hwi Bang, partial support for PI: Clive Randall) and DMR-2202525 (partial support for Clive Randall), and the Air Force Office of Scientific Research, grant number FA9550–19-1–0372 (postdoc funded: Arnaud Ndayishimiye; partial support for PI: Clive Randall). Also thanks to the facilities within the Materials Research Institute and the staff of the Materials Characterization Laboratory at Penn State University.

Experimental Approaches

Different experimental conditions will be shown in supplementary data. For others, we will simply redirect to the references with more detailed information.

References

[1] R.M. German, Sintering Theory and Practice, Wiley, New York, 1996.
[2] P.B. Vandiver, O. Soffer, B. Klima, J. Svoboda, Science 246 (1989) 1002.
[3] R.F. Walker, J.Am Ceram, Soc 38 (1955) 187.
[4] R.M. German, P. Suri, S.J. Park, J. Mater. Sci. 44 (2009) 1.
[5] R.E. Jaeger, L. Egerton, J. Am. Ceram. Soc. 45 (1962) 209.
[6] G. Goglio, A. Ndayishimiye, A. Largeteau, C. Elissalde, Scr. Mater. 158 (2019) 146.
[7] N. Yamasaki, K. Yanagisawa, M. Nishioka, S. Kanahara, J. Mater. Sci. Lett. 5 (1986) 355.
[8] S.-I. Hirano, S. So¯miya, J. Am. Ceram. Soc. 59 (1976) 534.
[9] H. Toraya, M. Yoshimura, S. So¯miya, J. Am. Ceram. Soc. 65 (1982) 159.
[10] S.J.L. Kang, Sintering (Oxford, Elsevier, Butterworth Heinemann, 2005).
[11] P.R. Cantwell, T. Frolov, T.J. Rupert, A.R. Krause, C.J. Marvel, G.S. Rohrer, J. M. Rickman, M.P. Harmer, Annu. Rev. Mater. Res. 50 (2020) 465.
[12] M.N. Rahaman, Ceramic Processing and Sintering, Taylor & Francis,, 2003.
[13] R.M. German, in: R.M. German (Ed.), Sinter. from Empir. Obs. to Sci. Princ, Butterworth-Heinemann, Boston, 2014, pp. 141–181.
[14] S.J.L. Kang, Sintering: Densification, Grain Growth and Microstructure. Elsevier Science, Oxford, 2004.
[15] J. Guo, H. Guo, A.L. Baker, M.T. Lanagan, E.R. Kupp, G.L. Messing, C.A. Randall, Angew. Chem. - Int. Ed. 55 (2016) 11457.
[16] C. Vakifahmetoglu, L. Karacasulu, Curr. Opin. Solid State Mater. Sci. 100807 (2020).
[17] A. Ndayishimiye, M.Y. Sengul, T. Sada, S. Dursun, S.H. Bang, Z.A. Grady, K. Tsuji, S. Funahashi, A.C.T. Van Duin, C.A. Randall, Open Ceram. 2 (2020), 100019.
[18] J. Guo, S.S. Berbano, H. Guo, A.L. Baker, M.T. Lanagan, C.A. Randall, Adv. Funct. Mater. 26 (2016) 7115.
[19] J.H. Seo, Z. Fan, H. Nakaya, R. Rajagopalan, E.D. Gomez, M. Iwasaki, C. A. Randall, J. Appl. Phys. 60 (2021) 37001.
[20] T. Ibn-Mohammed, C.A. Randall, K.B. Mustapha, J. Guo, J. Walker, S.S. Berbano, S.C.L. Koh, D. Wang, D.C. Sinclair, I.M. Reaney, J. Eur. Ceram. Soc. 39 (2019) 5213.
[21] S. Grasso, M. Biesuz, L. Zoli, G. Taveri, A.I. Duff, D. Ke, A. Jiang, M.J. Reece, Adv. Appl. Ceram. 1 (2020).
[22] F. Bouville, A.R. Studart, Nat. Commun. 8 (2017) 14655.
[23] H.C. Sorby, On the Direct Correlation of Mechanical and Chemical Forces (1863).
[24] K.B. Krauskopf, P. Karasek, L. Stavikova, J. Planeta, B. Hohnova´, M. Roth, K. R. ILER, W.K. Heidug, F. Renard, P. Ortoleva, J.P. Gratier, R.O. Fournier, J. J. Rowe, J.M.M. P´erez, J. Pascau, J. Geophys. Res. Solid Earth 100 (1995) 5931.
[25] R. Hellmann, P. Jean, Gratier, R. Guiguet, in *Water-Rock Interact. Ore Depos. Environ. Geochemistry A Tribut. to David A. Crerar*, The Geochemical Society, Special Publication,, 2002, pp. 129–152.
[26] F. Renard, P. Ortoleva, J.P. Gratier, Tectonophysics 280 (1997) 257.
[27] J.-P. Gratier, D.K. Dysthe, F. Renard, Adv. Geophys 54 (2013) 47.
[28] P.K. Weyl, J.Geophys Res 64 (1959) 2001.
[29] A. Polak, D. Elsworth, H. Yasuhara, A.S. Grader, P.M. Halleck, Geophys. Res. Lett. 30 (2003) 2003. GL017575.
[30] D.W. Durney, Nature 235 (1972) 315.
[31] E.H. Rutter, Tectonophysics 14 (1972) 13.

[32] E.H. Rutter, J. Geol, Soc. Lond. 140 (1983) 725.
[33] E.H. Rutter, Philos, Trans. R. Soc. Lond. Ser. A, Math. Phys. Sci. 283 (1976) 203.
[34] P.-Y.F. Robin, Geochim Cosmochim, Acta 42 (1978) 1383.
[35] T.J. McEwen, Contrib. Mineral. Pet. 67 (1978) 405.
[36] D. Durney, J.G. Ramsay, K.A. DeJong, and R. Scholten, (1973).
[37] B. Jamtveit, P. Meakin, in *Growth, Dissolution Pattern Form. Geosystems*, Springer,, Netherlands, Dordrecht, 1999, pp. 1–19.
[38] R.L. Stocker, M.F. Ashby, Rev. Geophys. 11 (1973) 391.
[39] G.M. Pharr, M.F. Ashby, Acta Met. 31 (1983) 129.
[40] R. Raj, C.K. Chyung, Acta Met. 29 (1981) 159.
[41] J.L. Urai, C.J. Spiers, H.J. Zwart, G.S. Lister, Nature 324 (1986) 554.
[42] C.J. Spiers, P.M.T.M. Schutjens, in *Deform. Process. Miner. Ceram. Rocks*, Springer,, Netherlands, Dordrecht, 1990, pp. 334–353.
[43] F.K. Lehner, J. Bataille, Pure Appl. Geophys. 122 (1985) 53.
[44] F.K. Lehner, Tectonophysics 245 (1995) 153.
[45] A. Niemeijer, C. Spiers, B. Bos, Earth Planet. Sci. Lett. 195 (2002) 261.
[46] A. Niemeijer, D. Elsworth, C. Marone, Earth Planet. Sci. Lett. 284 (2009) 386.
[47] E.E. Meyer, G.W. Greene, N.A. Alcantar, J.N. Israelachvili, J.R. Boles, J. Geophys. Res. 111 (2006) B08202.
[48] J.L. Urai, C.J. Spiers, H.J. Zwart, G.S. Lister, Nature 324 (1986) 554.
[49] F.K. Lehner, in *Deform. Process. Miner. Ceram. Rocks*, Springer,, Netherlands, Dordrecht, 1990, pp. 296–333.
[50] C.J. Spiers, P.M.T.M. Schutjens, R.H. Brzesowsky, C.J. Peach, J.L. Liezenberg, H. J. Zwart, Geol. Soc. Spec. Publ. 54 (1990) 215.
[51] A.M.H. Pluymakers, C.J. Spiers, Geol. Soc. Spec. Publ. 409 (2015) 107.
[52] H. Yasuhara, D. Elsworth, A. Polak, J. Geophys. Res. Solid Earth 108 (2003).
[53] M.S. Paterson, Rev Geophys 11 (1973) 355.
[54] H.J.M. Visser, C.J. Spiers, S.J.T. Hangx, J. Geophys. Res. B Solid Earth 117 (2012).
[55] T. Sada, A. Ndayishimiye, Z. Fan, Y. Fujioka, C.A. Randall, J. Appl. Phys. 129 (2021).
[56] X. Zhang, C.J. Spiers, Geochim. Cosmochim. Acta 69 (2005) 5681.
[57] X. Zhang, C.J. Spiers, C.J. Peach, J. Geophys. Res. Solid Earth 115 (2010) B09217.
[58] R. Raj, J.Geophys Res, Solid Earth 87 (1982) 4731.
[59] S. de Meer, J. Spiers, J. Geophys. Res. 102 (1997) 875.
[60] H.A. Janssen, Z.Ver Dtsch, Ing 39 (1895) 1045.
[61] H.M. Macleod, U. Marshall, Powder Technol. 16 (1977) 107.
[62] S. Leigh, J.E. Carless, B.W. Burt, J. Pharm. Sci. 56 (1967) 888.
[63] S. Abdel-Hamid, G. Betz, Drug Dev. Ind. Pharm. 37 (2011) 387.
[64] W.M. Long, Powder Met. 3 (1960) 73.
[65] J.S. Reed, Introduction to the Principles of Ceramic Processing, Wiley and Sons,, New York, 1988.
[66] R.A. Thompson, A. Ceram, Bull 60 (1981) 237.
[67] S.H. Bang, A. Ndayishimiye, C.A. Randall, J. Mater. Chem. C. 8 (2020) 5668.
[68] E.A. Meulenkamp, J. Phys. Chem. B 102 (1998) 7764.
[69] M.Y. Sengul, J. Guo, C.A. Randall, A.C.T. Van Duin, Angew. Chem. - Int. Ed. 58 (2019) 12420.
[70] S. Funahashi, H. Guo, J. Guo, A.L. Baker, K. Wang, K. Shiratsuyu, C.A. Randall, J. Am. Ceram. Soc. 100 (2017) 3488.
[71] S.H. Bang, K. Tsuji, A. Ndayishimiye, S. Dursun, J. Seo, S. Otieno, C.A. Randall, J. Am. Ceram. Soc. jace. 16976 (2020).
[72] J.L. Woolfrey, M.J. Bannister, J. Am. Ceram. Soc. 55 (1972) 390.
[73] H. Gerischer, N. Song, Acta 37 (1992) 827.
[74] M. Hurs¸it, O. Laçin, H. Saraç, J. Taiwan Inst. Chem. Eng. 40 (2009) 6.
[75] E.V. Blinkova, E.I. Eliseev, Izv. Vyss. Uchebnykh Zaved. Tsvetnaya Metall. 8 (2005).
[76] J. Deng, Q. Sun, P. Lin, G. Song, S. Wen, J. Deng, D. Wu, Int. J. Metall. Mater. Eng. 1 (2015) 109.
[77] G.C. Nicholson, J.Am Ceram, Soc 48 (1965) 525.
[78] T.K. Gupta, J.A.C.R.L. Coble 225 (1990).
[79] S.K. Dutta, R.M. Spriggs, J. Am. Ceram. Soc. 53 (1970) 61.
[80] T. Senda, R.C. Bradt, J. Am. Ceram. Soc. 73 (1990) 106.
[81] J. Han, P.Q. Mantas, A.M.R. Senos, J. Eur. Ceram. Soc. 20 (2000) 2753.
[82] S.H. Bang, M.Y. Sengul, A. Ndayishimiye, A.C.T. van Duin, C.A. Randall, Mater. Today Chem. 24 (2022), 100925.
[83] M.Y. Sengul, C.A. Randall, A.C.T. Van Duin, ACS Appl. Mater. Interfaces 10 (2018) 37717.
[84] Z. Hu, D.J. Escamilla Ramírez, B.E. Heredia Cervera, G. Oskam, P.C. Searson, J. Phys. Chem. B 109 (2005) 11209.
[85] B. Ingham, R. Linklater, T. Kemmitt, J. Phys. Chem. C. 115 (2011) 21034.
[86] N. Bouhssira, M.S. Aida, A. Mosbah, J. Cellier, J. Cryst. Growth 312 (2010) 3282.
[87] R. Viswanatha, P.K. Santra, C. Dasgupta, D.D. Sarma, Phys. Rev. Lett. 98 (2007), 255501.
[88] S.L. Cheng, J.H. Syn, S.Y. Liao, C.F. Lin, P.Y. Yeh, RSC Adv. 5 (2015) 67752.
[89] S. Liu, C.R. Liu, Cryst. Growth Des. 19 (2019) 2912.
[90] A. Ndayishimiye, Z. Fan, S. Funahashi, C.A. Randall, Inorg. Chem. 60 (2021) 13453.
[91] S. Takajo, W.A. Kaysser, G. Petzow, Acta Metall. Mater. 32 (1984) 107.
[92] M.P.A. van den Ende, A.R. Niemeijer, C.J. Spiers, J. Geophys. Res. Solid Earth 124 (2019) 10210.
[93] S. de Meer, C.J. Spiers, S. Nakashima, Earth Planet. Sci. Lett. 232 (2005) 403.
[94] R. van Noort, C.J. Spiers, G.M. Pennock, J. Geophys. Res. Solid Earth 113 (2008) 1.
[95] A. Ndayishimiye, M.Y. Sengul, S.H. Bang, K. Tsuji, K. Takashima, T. H´erisson de Beauvoir, D. Denux, J.-M. Thibaud, A.C.T. van Duin, C. Elissalde, G. Goglio, C. A. Randall, J. Eur. Ceram. Soc. 40 (2020) 1312.
[96] A. Ndayishimiye, Z.A. Grady, K. Tsuji, K. Wang, S.H. Bang, C.A. Randall, J. Am. Ceram. Soc. 103 (2020) 3039.
[97] T. Sada, Z. Fan, A. Ndayishimiye, K. Tsuji, S.H. Bang, Y. Fujioka, C.A. Randall, J. Am. Ceram. Soc. 104 (2021) 96.
[98] B.K. Lee, S.Y. Chung, S.J.L. Kang, Acta Mater. 48 (2000) 1575.
[99] A. Ndayishimiye, M.Y. Sengul, D. Akbarian, Z. Fan, K. Tsuji, S.H. Bang, A.C.T. van Duin, C.A. Randall, Nano Lett. 21 (2021) 3451.
[100] K. Tsuji, A. Ndayishimiye, S. Lowum, R. Floyd, K. Wang, M. Wetherington, J. P. Maria, C.A. Randall, J. Eur. Ceram. Soc. 40 (2020) 1280.
[101] A.J. Allen, I. Levin, R.A. Maier, S.E. Witt, F. Zhang, I. Kuzmenko, J. Am. Ceram. Soc. 104 (2021) 2442.
[102] R. Lu, C. Cheng, T. Nagel, H. Milsch, H. Yasuhara, O. Kolditz, H. Shao, Geomech. Geophys. Geo-Energy Geo-Resour. 7 (2021) 1.
[103] T. Herisson de Beauvoir, V. Villemot, M. Josse, Solid State Sci. 102 (2020).
[104] T. H´erisson de Beauvoir, A. Sangregorio, I. Cornu, C. Elissalde, M. Josse, J. Mater. Chem. C. 6 (2018) 2229.
[105] T. H´erisson de Beauvoir, F. Molinari, U.C. Chung-Seu, D. Michau, D. Denux, M. Josse, J. Eur. Ceram. Soc. 38 (2018) 3867.
[106] L. Paradis, D. Waryoba, K. Robertson, A. Ndayishimiye, Z. Fan, R. Rajagopalan, C. A. Randall, Adv. Eng. Mats. (2022), https://doi.org/10.1002/adem.202200714.
[107] S.M. Lowum, Ultralow-Temperature Densification of Ceramic, Ionic and Hybrid Materials via Cold Sintering and Cold Flow, The Pennsylvania State University, 2021.
[108] M. Biesuz, S. Grasso, V.M. Sglavo, Curr. Opin. Solid State Mater. Sci. 24 (2020), 100868.
[109] J. Gonzalez-Julian, K. Neuhaus, M. Bernemann, J. Pereira da Silva, A. Laptev, M. Bram, O. Guillon, Acta Mater. 144 (2018) 116.
[110] T. H´erisson de Beauvoir, A. Sangregorio, A. Bertrand, C. Payen, D. Michau, U. Chung, Ceram. Int. 45 (2019) 9674.
[111] J. Nie, Y. Zhang, J.M. Chan, R. Huang, J. Luo, Scr. Mater. 142 (2018) 79.
[112] J. Liang, S. Kang, X. Zhao, J. Guo, Z. Chen, J. Sun, L. Yang, R. Liao, C.A. Randall, J. Eur. Ceram. Soc. 42 (13) (2022) **5738–5746**.